Commun. Comput. Phys.
doi: 10.4208/cicp.060510.150511s

Vol. **11**, No. 4, pp. 1279-1299
April 2012

A Parallel Domain Decomposition Algorithm for Simulating Blood Flow with Incompressible Navier-Stokes Equations with Resistive Boundary Condition

Yuqi Wu[1,*] and Xiao-Chuan Cai[2]

[1] *Department of Applied Mathematics, University of Colorado at Boulder, Boulder, CO 80309, USA.*
[2] *Department of Computer Science, University of Colorado at Boulder, Boulder, CO 80309, USA.*

Received 15 May 2010; Accepted (in revised version) 15 May 2011

Available online 30 November 2011

Abstract. We introduce and study a parallel domain decomposition algorithm for the simulation of blood flow in compliant arteries using a fully-coupled system of nonlinear partial differential equations consisting of a linear elasticity equation and the incompressible Navier-Stokes equations with a resistive outflow boundary condition. The system is discretized with a finite element method on unstructured moving meshes and solved by a Newton-Krylov algorithm preconditioned with an overlapping restricted additive Schwarz method. The resistive outflow boundary condition plays an interesting role in the accuracy of the blood flow simulation and we provide a numerical comparison of its accuracy with the standard pressure type boundary condition. We also discuss the parallel performance of the implicit domain decomposition method for solving the fully coupled nonlinear system on a supercomputer with a few hundred processors.

AMS subject classifications: 74F10, 65M55, 35R37, 65Y05, 68W10

Key words: Fluid-structure interaction, blood flow, mesh movement, resistive boundary condition, additive Schwarz, domain decomposition, parallel computing.

1 Introduction

Artery diseases, such as the plaque formation, are closely related to flow properties of the blood and to the interaction between the blood and the artery walls. Different from the

*Corresponding author. *Email addresses:* yuqi.wu@colorado.edu (Y. Wu), cai@cs.colorado.edu (X.-C. Cai)

traditional experimental approach, the computational approach has the ability to simulate the velocity and pressure fields in a virtual environment, which is important in predicting the development of the disease and helps the treatment of the diseases [30]. Unfortunately, computer modeling of blood flow in arteries is a challenging problem [31]. In this paper, we develop a parallel fluid-structure interaction algorithm for the simulation of blood flow in compliant arteries using a fully-coupled system of partial differential equations.

One of the main challenges is the effective coupling of the fluid and the wall deformability. Two well-known formulations for the fluid-structure coupling are iterative and monolithic. In iterative approaches, the fluid, solid equations are solved sequentially, update each other's boundary conditions, until some desired tolerance is reached [17,26]. This enables the use of existing well-established fluid and structure solvers. However, difficulties in the form of lack of convergence have been addressed in a number of situations [24,28]. In monolithic approaches, the fluid, solid and mesh movement equations are solved simultaneously in fully-coupled fashion, where the coupling conditions enforced strongly as part of the system [3–6,19,23]. The fully-coupled approach shows to be more robust. Many of the convergence problems encountered within the iterative approach can be avoided with the monolithic approach [4]. Of course, there is a price to pay in this approach, solving the fully-coupled system is more computationally expensive. In this paper, we use the monolithic approach within the ALE framework.

In the blood flow simulation, the size and complexity of the circulation precludes a computational representation for the complete circuit in human body. Numerical models must invariably be truncated and divided into the upstream domain (modeled domain) and the downstream domain. And appropriate outflow boundary condition must be specified for the modeled domain. The downstream domain includes a vast quantities of smaller arteries, arterioles, capillaries, venules and veins returning blood to the heart. As a consequence, solutions to the governing equations of blood flow in the modeled domain depend closely on the outflow boundary conditions imposed to represent the influence from the downstream vascular system. By ignoring the effect of the downstream circulation, these boundary conditions may result in inaccurate predictions of velocity and pressure fields. In [16,32,33], a suggested solution is to use a reduced dimensional model to represent the downstream vessels and provide boundary conditions for the higher dimensional upstream model, where high-resolution information is needed.

In [4], Barker and Cai successfully developed a scalable parallel method for fluid-structure interaction problem. However, their model only use zero-traction as outlet boundary conditions. The blood pressure is not computed accurately from reports [33] and reference therein. For this reason, this paper describes the extension of Barker's paper to the following two aspects.

• In this paper, a more physically realistic outflow boundary condition is considered, namely the resistance of the flow. Where we assume the pressure P is a constant over the upstream outlets, the relation $P=QR$, representing the resistance to the flow of the down-

stream domain [18,25], is implicitly prescribed on the outflow boundary as the boundary condition, where $Q = \int_{\Gamma_{out}} \mathbf{u} \cdot \mathbf{n} ds$ represents the flow rate at the outflow boundary and R is the measured resistance. And we demonstrate its accuracy of the prediction of velocity and pressure fields by comparisons to the one using the zero-traction outflow boundary condition.

• The other goal of this paper is to understand the impact of the decomposition of the integral condition on the convergence and the scalability of the Schwarz preconditioned linear Jacobian solver. In the Newton-Krylov-Schwarz method, an inexact Newton method with line search is used as a nonlinear solver and within a Newton step, the linear Jacobian system is solved by GMRES preconditioned by an overlapping additive Schwarz preconditioner. With the traction boundary condition, the Jacobian matrix is uniformly sparse and the variables have local dependency, i.e., each variable is related through the function only to the neighboring variables. However, in the case of the resistive boundary condition, the Jacobian matrix has a dense block corresponding to the variables on the outlet boundaries due to the integral nature of the resistive boundary condition. As far as we know, the class of overlapping Schwarz methods had been successfully employed to the first kind of boundary condition [3,7,21], but as for the resistance boundary condition, the decomposition of the global domain into subdomains will break the integral connection between the variables on the outflow boundary, making the convergence and performance of this preconditioner interesting to discuss with.

We should also mention that we will only consider a 2D model in this paper. Although not completely physically realistic for blood flow simulations, this simplified 2D problem maintains all the mathematical aspect of the fully coupled fluid-structure interaction problem and also the ability to reproduce the important physical aspects of blood flow in complaint arteries.

The rest of the paper is organized as follows. In Section 2, we analyze the formulation of the fluid-structure interaction problem, including the strong and weak forms and the discretization of the problem, both in space and time. Then, in Section 3, we present the Newton-Krylov-Schwarz method with overlapping additive Schwarz preconditioner that we use to solve the nonlinear fully-coupled system. In Section 4, we demonstrate our algorithm on some artery models and report the parallel performance of our algorithm.

2 Formulation of the fluid-structure interaction problem

In the simulation of blood flow in compliant artery, the elastic vessel wall deforms in response of the blood pulse. The moving artery walls imply a moving fluid domain in turn. With the emphasize in tight and monolithic coupling for the fluid-structure, an additional field of solution variable and the governing equations for this field are introduced for modeling the deformation of the computational mesh in the fluid domain. As a result, our fluid-structure model couples the three components, the fluid, the elastic wall structure and the moving mesh. That is, we model the wall structure as linear elastic

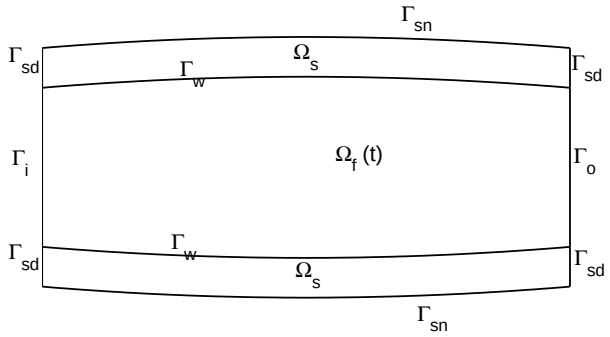

Figure 1: Ω_s is the structure domain in the Lagrangian reference configuration; $\Omega_0=\Omega_f(0)$ is the reference configuration of the fluid domain and $\Omega_f(t)$ represents the moving fluid domain at time t. The boundary to the structure domain is divided into a Dirichlet portion Γ_{sd} at the inlets and outlets and a Neumann portion Γ_{sn}. Γ_i and Γ_o are the inlet and outlet boundaries for the fluid domain. Γ_w represents the fluid-structure interface.

material in the Lagrangian frame, the fluid as viscous incompressible Newtonian flow in the arbitrary Lagrangian-Eulerian (ALE) framework [11,14,15,20] and the moving mesh for the ALE formulation. See Fig. 1 for a schematic and some notations.

Since the fluid domain is moving, the governing equations of the fluid need to be modified in the ALE framework. In the ALE framework, a mapping A_t is defined from the reference configuration $\Omega_f(0)$ to the moving domain $\Omega_f(t)$:

$$A_t:\quad \Omega_f(0)\to\Omega_f(t),\quad \mathbf{x}(Y,t)=A_t(\mathbf{Y}),\quad \forall\mathbf{Y}\in\Omega_f(0),$$

where $\mathbf{Y}$ is referred to as the ALE coordinate and $\mathbf{x}$ as the Eulerian coordinates. And a generic conservation law defined on a moving domain $\Omega_f(t)$

$$\frac{\partial u}{\partial t}+\nabla_{\mathbf{x}}\cdot F(u)=f$$

can be written in the ALE form as

$$\frac{\partial u}{\partial t}\Big|_{\mathbf{Y}}-\omega\cdot\nabla_{\mathbf{x}}u+\nabla_{\mathbf{x}}\cdot F(u)=f,\quad \text{in } \Omega_f(t),$$

where $\omega=\partial A_t/\partial t$ is the velocity of the moving mesh and Y indicates that the time derivative is taken with respect to the ALE coordinates.

The fully coupled fluid-structure interaction problem is given by

$$\rho_s\frac{\partial^2\mathbf{x}_s}{\partial t^2}-\nabla\cdot\sigma_s-\beta\frac{\partial(\Delta\mathbf{x}_s)}{\partial t}+\gamma\mathbf{x}_s=\mathbf{f}_s,\qquad \text{in } \Omega_s, \tag{2.1a}$$

$$\mathbf{x}_s=0,\qquad \text{on } \Gamma_{sd}, \tag{2.1b}$$

$$\frac{\partial\mathbf{u}_f}{\partial t}\Big|_Y+\left[(\mathbf{u}_f-\omega_g)\cdot\nabla\right]\mathbf{u}_f+\frac{1}{\rho_f}\nabla p_f=\nu_f\Delta\mathbf{u}_f+\mathbf{f}_f,\qquad \text{in } \Omega_f(t), \tag{2.1c}$$

$$\nabla\cdot\mathbf{u}_f=0, \qquad \text{in } \Omega_f(t), \tag{2.1d}$$

$$\mathbf{u}_f=g, \qquad \text{on } \Gamma_i, \tag{2.1e}$$

$$p_f=RQ=R\int_{\Gamma_o}\mathbf{u}_f\cdot\mathbf{n}_f ds, \qquad \text{on } \Gamma_o, \tag{2.1f}$$

$$\Delta\mathbf{x}_f=0, \qquad \text{in } \Omega_0, \tag{2.1g}$$

$$\mathbf{x}_f=0, \qquad \text{on } \Gamma_i\cup\Gamma_o. \tag{2.1h}$$

In (2.1a) and (2.1b), $\mathbf{x}_s$ describes the displacement of solid motion and $\sigma_s=\lambda_s(\nabla\cdot\mathbf{x}_s)I+\mu_s(\nabla\mathbf{x}_s+\nabla\mathbf{x}_s^T)$ is the Cauchy stress tensor. The Lamé parameters λ_s and μ_s are characterized by $\lambda_s=\nu_sE/((1+\nu_s)(1-2\nu_s))$, $\mu_s=E/(2(1+\nu_s))$, where E is the Young's modulus and ν_s is the Poisson ratio, ρ_s is the solid density, β is a visco-elastic damping parameter and the γ term is used to represent a radially symmetric artery in two dimensions [1]. While in (2.1c)-(2.1f), $\mathbf{u}_f$ and p_f represent the fluid velocity and the pressure, respectively. ρ_f is the fluid density, ν_f is the kinematic viscosity and $\omega_g=\partial\mathbf{x}_f/\partial t$ is the velocity of the moving mesh. In order to describe the moving mesh, the fluid mesh displacements $\mathbf{x}_f$ are made to satisfy a harmonic extension of the moving fluid-structure interface by (2.1g) and (2.1h).

In addition to the above governing equations and boundary conditions, more importantly, the coupling conditions at the fluid-structure interface need to be specified. In our fully coupled setting, three coupling conditions must be satisfied at the fluid-structure interface Γ_w corresponding to the structure, fluid and moving mesh equations

$$\sigma_s\cdot\mathbf{n}_s=-\sigma_f\cdot\mathbf{n}_f, \tag{2.2a}$$

$$\mathbf{u}_f=\frac{\partial\mathbf{x}_s}{\partial t}, \tag{2.2b}$$

$$\mathbf{x}_f=\mathbf{x}_s, \tag{2.2c}$$

where $\mathbf{n}_s$, $\mathbf{n}_f$ are unit normal vectors for the solid and fluid at the fluid-structure interface respectively and σ_s and $\sigma_f=-p_fI+\rho_f\nu_f(\nabla\mathbf{u}_f+\nabla\mathbf{u}_f^T)$ are the Cauchy stress tensors for the solid and fluid respectively.

We next introduce the weak formulation of the fully coupled fluid-structure interaction problem. Consider the coupling condition (2.2a) and boundary conditions, we define the variational space of the structure problem as:

$$X=\left\{\mathbf{x}_s\in[H^1(\Omega_s)]^2:\ \mathbf{x}_s=0 \text{ on } \Gamma_{sd}\right\}.$$

The weak form of the structure problem is stated as follows: Find $\mathbf{x}_s\in X$ such that $\forall\phi_s\in X$,

$$B_s(\mathbf{x}_s,\phi_s;\sigma_f)=F_s(\phi_s), \tag{2.3}$$

where

$$B_s(\mathbf{x}_s,\phi_s;\sigma_f)=\rho_s\frac{\partial^2}{\partial t^2}\int_{\Omega_s}\mathbf{x}_s\cdot\phi_s d\Omega+\int_{\Omega_s}\nabla\phi_s:\sigma_s d\Omega+\beta\frac{\partial}{\partial t}\int_{\Omega_s}\nabla\phi_s:\mathbf{x}_s d\Omega$$
$$+\gamma\int_{\Omega_s}\mathbf{x}_s\cdot\phi_s d\Omega-\int_{\Gamma_w}\phi_s\cdot(\sigma_f\cdot\mathbf{n}_s)ds, \tag{2.4}$$

$$F_s(\phi_s)=\int_{\Omega_s}\mathbf{f}_s\cdot\phi_s d\Omega, \tag{2.5}$$

where we replace $\sigma_s\cdot\mathbf{n}_s$ with $\sigma_f\cdot\mathbf{n}_s$ in (2.4) by virtue of the coupling relation (2.2a) on the interface Γ_w.

The variational spaces of the fluid subproblem are time-dependent and the solution of the structure subproblem provides an essential boundary condition for the fluid subproblem by (2.2b). We define the trial solution and weighting function spaces as:

$$V=\Big\{\mathbf{u}_f\in[H^1(\Omega_f(t))]^2:\ \mathbf{u}_f=g\ \text{ on }\ \Gamma_i,\ \mathbf{u}_f=\frac{\partial\mathbf{x}_s}{\partial t}\ \text{ on }\ \Gamma_w\Big\},$$
$$V_0=\Big\{\mathbf{u}_f\in[H^1(\Omega_f(t))]^2:\ \mathbf{u}_f=0\ \text{ on }\ \Gamma_i\cup\Gamma_w\Big\},\qquad P=L^2(\Omega_f(t)).$$

The weak form of the fluid problem reads: Find $\mathbf{u}_f\in V$ and $p_f\in P$ such that $\forall\phi_f\in V_0$ and $\forall\psi_f\in P$,

$$B_f\big(\{\mathbf{u}_f,p_f\},\{\phi_f,\psi_f\};\omega_g\big)=F_f\big(\{\phi_f,\psi_f\}\big), \tag{2.6}$$

where

$$B_f\big(\{\mathbf{u}_f,p_f\},\{\phi_f,\psi_f\};\omega_g\big)$$
$$=\int_{\Omega_f(t)}\frac{\partial\mathbf{u}_f}{\partial t}\Big|_Y\cdot\phi_f d\Omega+\int_{\Omega_f(t)}\big[(\mathbf{u}_f-\omega_g)\cdot\nabla\big]\mathbf{u}_f\cdot\phi_f d\Omega+\nu_f\int_{\Omega_f(t)}\nabla\mathbf{u}_f:\nabla\phi_f d\Omega$$
$$-\int_{\Omega_f(t)}p_f(\nabla\cdot\phi_f)d\Omega+\int_{\Omega_f(t)}(\nabla\cdot\mathbf{u}_f)\psi_f d\Omega-\int_{\Gamma_o}\mathbf{t}_f\cdot\phi_f ds, \tag{2.7}$$

where $t_f=-p\mathbf{n}_f+\nu_f(\nabla\mathbf{u}_f\cdot\mathbf{n}_f)$ and

$$F_f\big(\{\phi_f,\psi_f\}\big)=\int_{\Omega_f(t)}\mathbf{f}_f\cdot\phi_f d\Omega. \tag{2.8}$$

The last term in (2.7) representing the contribution of the resistance boundary condition on the outlet Γ_o can be modified as:

$$\int_{\Gamma_o}\mathbf{t}_f\cdot\phi_f ds=-\int_{\Gamma_o}\Big(R\int_{\Gamma_o}\mathbf{u}_f\cdot\mathbf{n}_f ds\Big)\phi_f\cdot\mathbf{n}_f ds+\nu_f\int_{\Gamma_o}\phi_f\cdot(\nabla\mathbf{u}_f)\cdot\mathbf{n}_f ds \tag{2.9}$$

thanks to the relation (2.1f).

We define the variational spaces of the mesh movement as:

$$Z_0=\Big\{\mathbf{x}_f\in[H^1(\Omega_0)]^2:\ \mathbf{x}_f=0\ \text{ on }\ \Gamma_i\cup\Gamma_o\cup\Gamma_w\Big\},$$
$$Z=\Big\{\mathbf{x}_f\in[H^1(\Omega_0)]^2:\ \mathbf{x}_f=\mathbf{x}_s\ \text{ on }\ \Gamma_w,\ \mathbf{x}_f=0\ \text{ on }\ \Gamma_i\cup\Gamma_o\Big\}.$$

The weak form of the mesh movement problem reads: Find $\mathbf{x}_f\in Z$ such that $\forall\xi\in Z_0$

$$B_m(\mathbf{x}_f,\xi)=0, \tag{2.10}$$

where

$$B_m(\mathbf{x}_f,\xi)=\int_{\Omega_0}\nabla\xi:\nabla\mathbf{x}_f d\Omega. \tag{2.11}$$

We use an unstructured finite element method to discretize the fully coupled fluid-structure interaction problem in space, using the LBB-stable mixed Q2-Q1 elements for the fluid and Q2 elements for the structure. Denote the finite element subspaces X_h, V_h, $V_{h,0}$, P_h, Z_h, $Z_{h,0}$ as the counterparts of their infinite dimensional subspaces. We approximate the fully coupled fluid-structure interaction problem as: Find $x_s\in X_h$, $u_f\in V_h$, $p_f\in P_h$ and $x_f\in Z_h$ such that $\forall\phi_s\in X_h$, $\forall\phi_f\in V_{h,0}$, $\forall\psi_f\in P_h$ and $\forall\xi\in Z_{h,0}$,

$$B_s\big(\mathbf{x}_s,\phi_s;\sigma_f\big)-F_s(\phi_s)+B_f\big(\{\mathbf{u}_f,p_f\},\{\phi_f,\psi_f\};\omega_g\big)-F_f\big(\{\phi_f,\psi_f\}\big)+B_m(\mathbf{x}_f,\xi)=0 \tag{2.12}$$

with the discretized version of coupling conditions (2.2b) and (2.2c). Representing the traction coupling condition (2.2a), the operator B_s has linear dependency to the fluid velocity u_f and pressure p_f as described in the boundary term of (2.3). Since we model the fluid in the ALE framework, the integration domain $\Omega_f(t)$ in (2.7) depends implicitly on the mesh displacement x_f and the convection term that appears in (2.7) depends on both u_f and x_f. As a consequence, the operator B_f depends on x_f and u_f nonlinearly.

By introducing the structure velocity $\dot{x}_s$ as an additional unknown variable, we change the equation to a first-order system, rewriting B_s as:

$$\begin{aligned}B_s\big(\{x_s,\dot{x}_s\},\{\phi_s,\varphi_s\};\sigma_f\big)=&\rho_s\frac{\partial}{\partial t}\int_{\Omega_s}\dot{x}_s\cdot\phi_s d\Omega+\int_{\Omega_s}\nabla\phi_s:\sigma_s d\Omega+\beta\int_{\Omega_s}\nabla\phi_s:\dot{x}_s d\Omega\\&+\gamma\int_{\Omega_s}x_s\cdot\phi_s d\Omega-\int_{\Gamma_w}\phi_s\cdot(\sigma_f\cdot\mathbf{n}_s)ds+\int_{\Omega_s}\Big(\frac{\partial x_s}{\partial t}-\dot{x}_s\Big)\cdot\varphi_s d\Omega,\end{aligned} \tag{2.13}$$

where $\dot{x}_s$ and φ_s are in X_h.

Discretizing in time with the second-order implicit trapezoidal rule to both the fluid and structure, the fully coupled nonlinear system arrives:

$$\mathcal{F}(y^{n+1})=\mathcal{L}(y^{n+1})-\frac{\Delta t}{2}\mathcal{B}(y^{n+1})-\mathcal{L}(y^n)-\frac{\Delta t}{2}\mathcal{B}(y^n)=0, \tag{2.14}$$

where $y^n=(u_f^n\ p_f^n\ x_f^n\ x_s^n\ \dot{x_s}^n)^T$ is the solution at the time step t_n. And we define

$$\mathcal{L}(y^n)=\rho_s\int_{\Omega_s}\dot{x}_s^n\cdot\phi_s d\Omega+\int_{\Omega_s}x_s^n\cdot\varphi_s d\Omega+\int_{\Omega_f(t)}u_f^n\cdot\phi_f d\Omega, \tag{2.15a}$$

$$\mathcal{B}(y^n)=-\big(\mathcal{B}_s(y^n)+\mathcal{B}_f(y^n)+\mathcal{B}_m(y^n)\big), \tag{2.15b}$$

$$\begin{aligned}\mathcal{B}_s(y^n)=&\int_{\Omega_s}\nabla\phi_s:\sigma_s^n d\Omega+\beta\int_{\Omega_s}\nabla\phi_s:\dot{x}_s^n d\Omega+\gamma\int_{\Omega_s}x_s^n\cdot\phi_s d\Omega-\int_{\Gamma_w}\phi_s\cdot(\sigma_f^n\cdot\mathbf{n}_s)ds\\&-\int_{\Omega_s}\dot{x}_s^n\cdot\varphi_s d\Omega-\int_{\Omega_s}f_s^n\cdot\phi_s d\Omega,\end{aligned} \tag{2.15c}$$

$$\begin{aligned}\mathcal{B}_f(y^n)=&\int_{\Omega_f(t)}[(u_f^n-\omega_g^n)\cdot\nabla]u_f^n\cdot\phi_f d\Omega+\nu_f\int_{\Omega_f(t)}\nabla u_f^n:\nabla\phi_f d\Omega-\int_{\Gamma_o}\mathbf{t}_f^n\cdot\phi_f ds\\&-\int_{\Omega_f(t)}p_f^n(\nabla\cdot\phi_f)d\Omega+\int_{\Omega_f(t)}(\nabla\cdot u_f^n)\psi_f d\Omega-\int_{\Omega_f(t)}f_f^n\cdot\phi_f d\Omega,\end{aligned} \tag{2.15d}$$

$$\mathcal{B}_m(y^n)=\int_{\Omega_0}\nabla\xi:\nabla x_f^n d\Omega. \tag{2.15e}$$

Since our temporal discretization scheme is fully-implicit, in order to obtain the solution y^{n+1} for the current time step $t_{n+1}=(n+1)\Delta t$, we need to solve the nonlinear system (2.14).

3 Parallel Newton-Krylov-Schwarz algorithm

The large size of the nonlinear fully-coupled system (2.14) demands for intensive computational power. A parallel scalable solver becomes a must in our simulation. In this paper, we employ a Newton-Krylov-Schwarz (NKS) algorithm [7, 21], in which an inexact Newton method with backtracking [12, 13] is used as the nonlinear solver. At each time step, let the initial guess $x^{(0)}$ be given as the solution of the previous time step and assume $x^{(k)}$ is the current approximation at the k^{th} Newton step. The approximation at the next Newton step $x^{(k+1)}$ is computed via

Step 1 Solve a preconditioned linear Jacobian system to find the Newton correction $s^{(k)}$, by using a Krylov subspace method, GMRES [29]

$$-M_k^{-1}J_k s^{(k)}=M_k^{-1}\mathcal{F}(x^{(k)}), \tag{3.1}$$

where J_k is the Jacobian matrix evaluated at $x^{(k)}$ and the left preconditioner M_k^{-1} is the overlapping additive Schwarz preconditioner, which we are going to discuss in details in this subsection later.

Step 2 Update the new approximation $x^{(k+1)}=x^{(k)}+\theta^{(k)}s^{(k)}$, where $\theta^{(k)}\in(0,1]$ is the step length parameter.

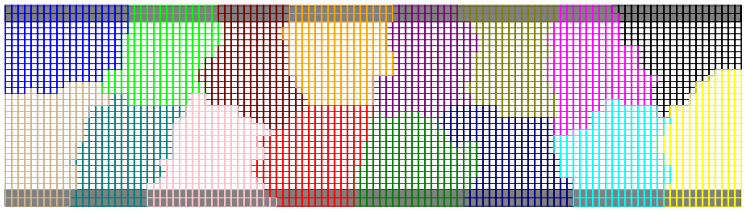

Figure 2: Example partition of the domain into 16 subdomains. The outlet boundary on the right is shared by two different subdomains.

In Step 1, the accuracy of the solution to the preconditioned Jacobian systems is controlled by the forcing term η_k,

$$\|M_k^{-1}(\mathcal{F}(x^{(k)})+J_k s^{(k)})\| \leq \eta_k \|M_k^{-1}\mathcal{F}(x^{(k)})\|. \tag{3.2}$$

In Step 2, if the correction $s^{(k)}$ gives adequate progress towards the solution, we keep this correction by making $\theta^{(k)}=1$. If not, then we obtain a conservative correction by choosing an appropriate step length $\theta^{(k)}$. In this situation, the step length, $\theta^{(k)} \in [\theta_{\min},\theta_{\max}] \subset (0,1)$ is chosen to insure

$$g(x^{(k)}+\theta^{(k)}s^{(k)}) \leq g(x^{(k)})+\alpha\theta^{(k)}\nabla g(x^{(k)})^T s^{(k)}, \tag{3.3}$$

where $g: R^n \to R$ is defined as $\|\mathcal{F}\|_2^2$ and the parameter α is a safeguard to assure sufficient reduction of g. In practice, a cubic line search technique [10] is employed to determine the step length $\theta^{(k)}$.

To define the restricted additive Schwarz preconditioner M_k^{-1} in (3.1), we first partition the finite element mesh $\mathcal{T}^h = \Omega_f^h \cup \Omega_s^h$ into non-overlapping subdomains Ω_ℓ^h, $\ell = 1,\cdots,N$. Each one corresponds to a processor of the parallel machine and their union covers the entire mesh $\mathcal{T}^h$. This partition preserves the integrity of the elements, that is, each subdomain Ω_ℓ^h consists of an integral number of elements. And the partition respects the fully coupled nature of fluid-structure interaction problem, disregarding the fluid-structure interface in the partition, that is, solid elements and fluid elements can be grouped into the same subdomain. Then, the subdomains Ω_ℓ^h are extended to overlapping domains $\Omega_\ell^{h,\delta}$, where δ represents the size of overlap in terms of layers of elements. The only criterion of the partition is to minimize the edge cuts, the outlet boundary may be cut into different subdomains, see Fig. 2. In such a situation, the global connection between variables on the outlet boundaries, which are established by the resistance boundary condition (2.1f), is destroyed. Now, we define the solution space as:

$$S^h = \left\{ (u_f,p_f,x_f,x_s,\dot{x}_s) : \ u_f \in V_h,\ p_f \in P_h,\ x_f \in Z_h,\ x_s \in X_h,\ \dot{x}_s \in X_h \right\} \tag{3.4}$$

and the subdomain solution spaces as:

$$S_\ell^{h,\delta}=\left\{(u_f,p_f,x_f,x_s,\dot{x}_s):\begin{array}{llll} u_f\in V_h\cap[H^1(\Omega_\ell^{h,\delta})]^2, & u_f=0 & \text{on} & (\partial\Omega_\ell^{h,\delta}\setminus\Gamma_o)\cap\Omega_f^h; \\ p_f\in P_h\cap H^1(\Omega_\ell^{h,\delta}), & p_f=0 & \text{on} & [\partial\Omega_\ell^{h,\delta}\setminus(\Gamma_o\cup\Gamma_i)]\cap\Omega_f^h; \\ x_f\in Z_h\cap[H^1(\Omega_\ell^{h,\delta})]^2, & x_f=0 & \text{on} & \partial\Omega_\ell^{h,\delta}\cap\Omega_f^h; \\ x_s\in X_h\cap[H^1(\Omega_\ell^{h,\delta})]^2, & x_s=0 & \text{on} & \partial\Omega_\ell^{h,\delta}\cap\Omega_s^h; \\ \dot{x}_s\in X_h\cap[H^1(\Omega_\ell^{h,\delta})]^2, & \dot{x}_s=0, & \text{on} & \partial\Omega_\ell^{h,\delta}\cap\Omega_s^h \end{array}\right\}.$$

And we present two restriction operators here, one preserves the global connection, while the other one does not.

- Choice 1, let $R_\ell:\ S^h\to S_\ell^{h,\delta}$ be the restriction operator, which returns all degrees of freedom associated with the subspace $S_\ell^{h,\delta}$, without preserving the global connection.
- Choice 2, let $R_\ell:\ S^h\to S_\ell^{h,\delta}\cup\{u_f(x,y):\ (x,y)\in\Gamma_o^h\}$ be the restriction operator, which returns all degrees of freedom in $S_\ell^{h,\delta}$ as well as the degrees of freedom corresponding to the velocity variables on the outlet boundary Γ_o. In this way, we manually extend the subdomains to preserve the global connection.

Using the restriction matrix, we write the one-level restricted additive Schwarz preconditioner [8] as

$$M_k^{-1}=\sum_{\ell=1}^{N}(R_\ell^0)^T J_\ell^{-1}R_\ell, \tag{3.5}$$

where J_ℓ is the subdomain operator of $J_\ell=R_\ell J R_\ell^T$. And R_ℓ^0 is a restriction to the degrees of freedom in the non-overlapping subdomain Ω_ℓ^h.

4 Numerical results

In this section, we study the application of our solver to a two-dimensional model of the pulmonary artery. We first focus on the impact of different outflow boundary conditions on the fluid velocity and pressure fields. We then investigate the performance of the Schwarz type preconditioner with respect to the integral type resistive outflow boundary condition. In the end, we discuss the parallel scalability and robustness of our solver, especially in the case of resistive outflow boundary condition. Our parallel code is implemented by using the Portable Extensible Toolkit for Scientific computation (PETSc) [2]. Mesh generation and partition are carried out by CUBIT [27] and ParMETIS [22], respectively. All the numerical results are obtained on an IBM BlueGene/L supercomputer at the National Center for Atmospheric Research with 4096 compute nodes.

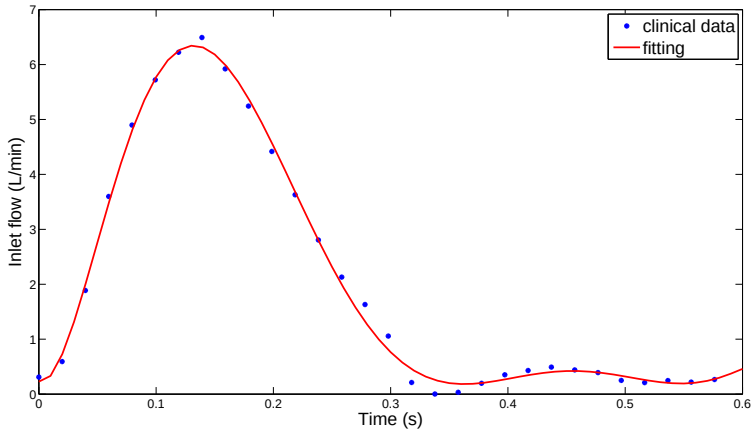

Figure 3: The inlet flow rate from clinical data after polynomial fitting.

4.1 Impact of different types of boundary conditions

In this test, we consider pulsatile flow in a straight compliant vessel with a prescribed inlet flow rate and different boundary conditions. The length and diameter of the artery are 20cm and 2cm, respectively. And the thickness of the artery wall is 0.2cm. For the inlet, we prescribe a pulsatile periodic flow wave, with a period T of 0.6s, mapped to a uniform velocity profile. The inlet flow rate is given in Fig. 3[†]. For the outlet, either zero-traction or resistance boundary condition is considered. The Young's modulus of the artery wall is $6.0\times10^5 \mathrm{g}/(\mathrm{cms}^2)$. Poisson ratio is 0.48 and the wall density is $1.2\mathrm{g}/\mathrm{cm}^3$. The blood is modeled as a Newtonian flow, with a density of $1.0\mathrm{g}/\mathrm{cm}^3$ and kinematic viscosity of $0.035\mathrm{cm}^2/\mathrm{s}$. The tests shown in this case are run on 256 processors and numerical solutions are obtained using a grid with 58369 elements and 1.01 million degrees of freedom with a time step of 1ms, for a total of 3 cardiac cycle. As for the initial condition, it is important that the fluid-structure interaction system starts from a equilibrium state [16]. Instead of prescribing zero initial for all variables, we obtain the initial condition as follows:

1. The velocity of the wall is initially set to zero.
2. A steady FSI problem is solved, using the same inlet and outlet boundary conditions as in the time-dependent problem. The velocity $u_{f,0}$, the pressure $p_{f,0}$, the fluid mesh displacement $x_{f,0}$, the solid displacement $x_{s,0}$ fields are obtained and then used as the initial conditions.

Fig. 4 depicts the results obtained with the resistance and zero-traction outflow boundary conditions. For the resistance boundary condition, the wall displacement plot follows the shape of the wall pressure plot, as one can see in the top right figure. Meaning that the

[†]The data is provided by Z. Su, K. Hunter and R. Shandas of University of Colorado, School of Medicine.

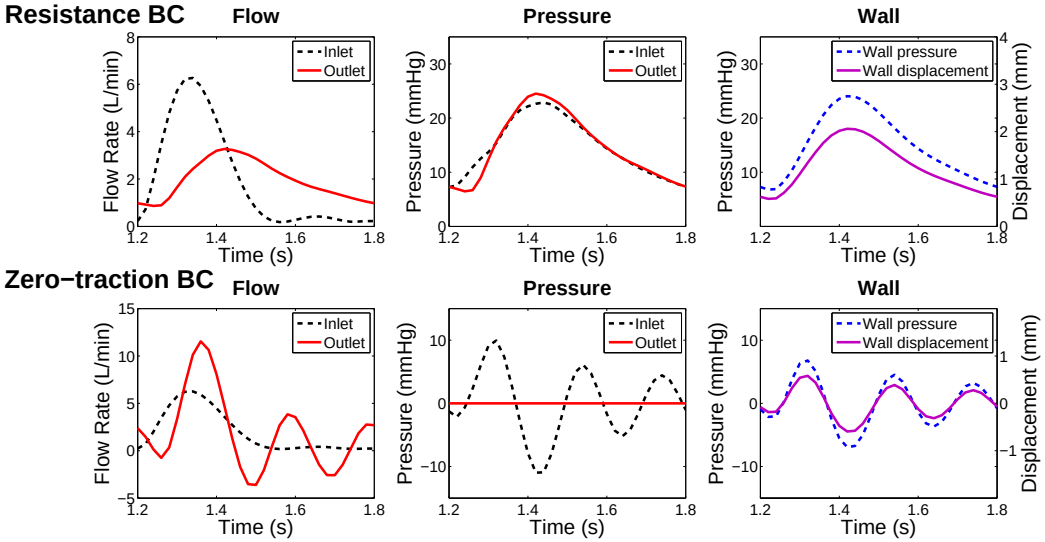

Figure 4: Flow waves, pressure at inlet and outlet, wall pressure and wall displacement of the artery model, obtained using resistance and zero-traction outlet boundary conditions. Top figures represent the inlet and outlet flow rate, inlet and outlet pressure and wall displacement and pressure (from left to right) by using resistance boundary condition, while the bottom figures represent the results by using the zero-traction outflow boundary condition.

artery walls dilate as the magnitude of pressure increases and contract as the magnitude of pressure decreases. The pressure pulse alters the flow distribution over the cardiac cycle, e.g., the outlet flow rate damps compared to the inlet flow rate at peak systole, while the outlet flow rate is larger than the inlet flow rate at diastole state. For the zero-traction boundary condition, both the flow wave and pressure are dramatically different from the resistance case. Unrealistic peak and negative flow are observed at the outlet. And the pressure in the zero-traction case fails to represent the physiologic pressure pulse, resulting in unrealistic amplitude and oscillatory pattern.

Fig. 5 displays the computed streamlines for the resistance boundary condition at two different phases, the peak systole and the mid-diastole $(t=5T/6)$. We can see the deformation of artery walls in response to the pulse of the flow. At the peak systole phase, the artery walls dilate so that the flow at the outlet damps. While at the mid-diastole phase, the flow is slower, the artery walls shrink and more flow is leaving than entering. We also observe that at the mid-diastole stage, some vortices are generated near the inlet boundary and the direction of the flow is reversed near the artery wall. Fig. 6 shows the computed streamlines for the zero traction boundary condition at the same phases. Compared to the resistance case, the flow pattern behaves differently and the wall deformation is smaller. At the mid-diastole phase, reserve flow is observed near the outlet boundary. Fig. 7 and Fig. 8 depict the computed pressure distribution at these two selected phases by using resistance outflow boundary condition and zero-traction outflow boundary condition, respectively.

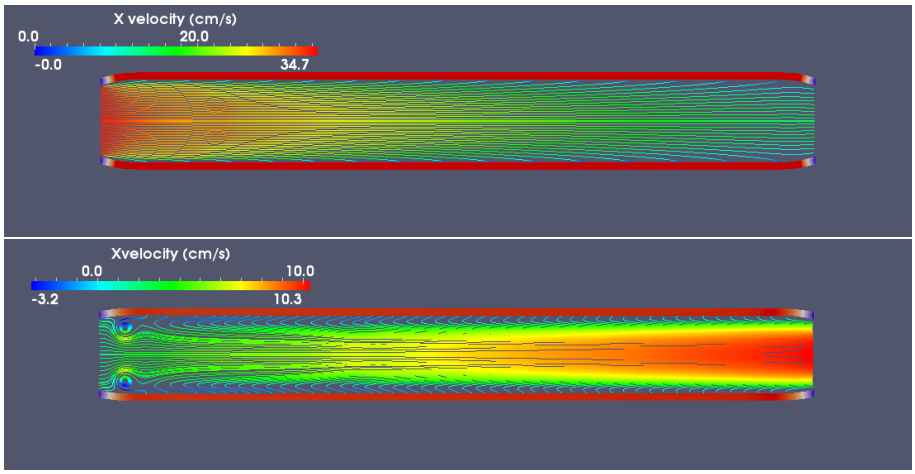

Figure 5: Streamlines at the peak systole and mid-diastole phases using the resistance outflow boundary condition. The artery walls are colored by the magnitude of the displacement and fluid streamlines are colored by the velocity in the X direction. The top figure represents the peak systole phase, the bottom figure for the mid-diastole phase.

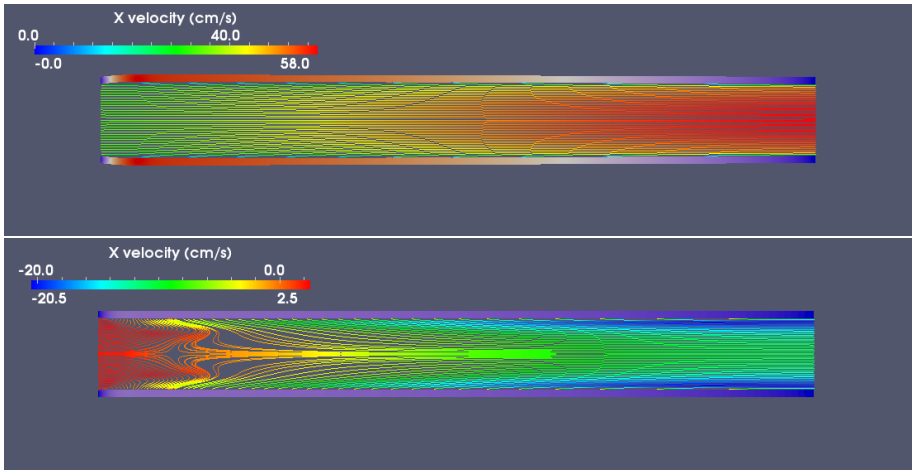

Figure 6: Streamlines at the peak systole and mid-diastole phases using the zero-traction outflow boundary condition. The artery walls are colored by the magnitude of the displacement and fluid streamlines are colored by the velocity in the X direction. The top figure represents the peak systole phase, the bottom figure for the mid-diastole phase.

So far, we have discussed the impact of the resistance outflow boundary condition and the zero-traction outflow boundary condition to the simulation of blood flow in complaint arteries. The resistance boundary condition is shown to be an improvement over the zero-traction outflow boundary condition.

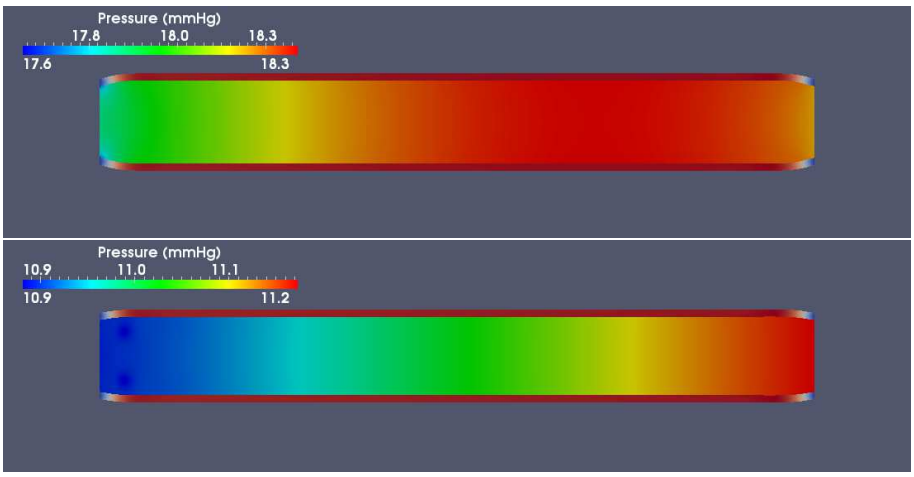

Figure 7: Pressure distribution at the peak systole and mid-diastole phases using the resistance outflow boundary condition. The artery walls are colored by the magnitude of the displacement. The top figure represents the peak systole phase, the bottom figure for the mid-diastole phase.

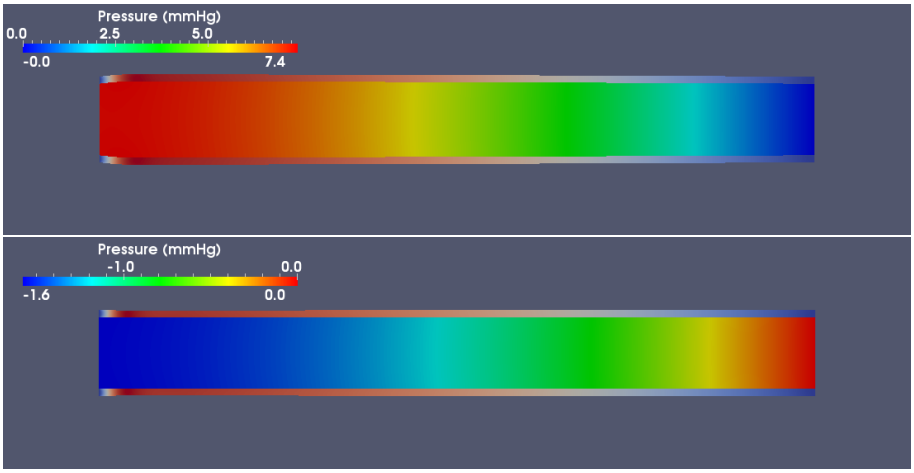

Figure 8: Pressure distribution at the peak systole and mid-diastole phases using the zero-traction outflow boundary condition. The artery walls are colored by the magnitude of the displacement. The top figure represents the peak systole phase, the bottom figure for the mid-diastole phase.

4.2 Scalability and performance

In this subsection, we study the performance and parallel scalability of our solver by using the same geometry and material properties as described before. In all the following tests, unless otherwise specified, we choose the time step $\Delta t = 1$ms. The accuracy of the preconditioned Jacobian system is controlled by the stopping condition $\eta_k = 10^{-4}$. The stopping criterion for the Newton iterations is when the residual of the nonlinear system is decreased by a factor of 10^{-6}. For all the performance and scalability results, we

Table 1: Comparison of the performance of our solver with two different restriction operators, using the resistance outflow boundary condition. The exact definition of Choice 1 and Choice 2 can be found in Section 3. np refers to the number of processors. The tests are carried on a fixed grid with 2.01×10^6 degrees of freedom and overlap $\delta=4$.

	Choice 1			Choice 2		
np	Newton	GMRES	time (s)	Newton	GMRES	time (s)
64	3.1	49.9	316.24	3.0	48.2	304.52
128	3.0	54.7	156.53	3.0	53.6	162.39
256	3.0	90.8	108.50	3.0	88.5	112.84
512	3.0	162.1	54.961	3.0	158.8	54.58

Table 2: Comparison of the performance of our solver with the zero-traction and resistance outflow boundary conditions. The tests are carried on a fixed grid with 2.01×10^6 degrees of freedom and overlap $\delta=4$.

	Zero-traction			Resistance		
np	Newton	GMRES	time	Newton	GMRES	time (s)
64	3.0	49.5	300.61	3.1	49.9	316.24
128	3.0	54.3	152.53	3.0	54.7	156.53
256	3.0	87.9	100.52	3.0	90.8	108.50
512	3.0	159.4	54.10	3.0	162.1	54.96

proceed 10 time steps and then report the average compute time and the average number of Newton iterations per time step and the average GMRES iterations per Newton step.

We first compare the performance of the restricted additive Schwarz (RAS) preconditioner with two different choices of restriction presented in Section 3 by using the resistance outflow boundary condition. Choice 1 represents the restriction to $S_\ell^{h,\delta}$, while Choice 2 represents the restriction which includes all velocity variables on the outlet boundary. As one can see from the results in Table 1, both choices handle the resistance outflow boundary condition well, guarantee the convergence and perform in a similar way. As the number of processors (np) increases, the number of GMRES iterations per Newton step increases and the compute time per time step decreases. Choice 2 uses fewer linear iterations compared to Choice 1, because it preserves the global connection structure at the outlet. However, in terms of compute time, it is hard to see the advantage. In the case of Choice 2, more communication is required, resulting in a larger total compute time. As a result, Choice 1 is our preferred restriction because it is easier to implement and also maintains a respectable convergence rate.

To further illustrate the performance of the restricted additive Schwarz preconditioner with the resistance outflow boundary condition, we compare its performance (using Choice 1 restriction) to the case when the zero-traction boundary condition is used. In the case of zero-traction boundary condition, the Jacobian matrix is uniformly sparse and the variables have only local dependency. In theory and practices, the performance of RAS with the zero-traction boundary condition has been successfully demonstrated. In Table 2, we observe that RAS handles the resistance boundary condition well. In terms

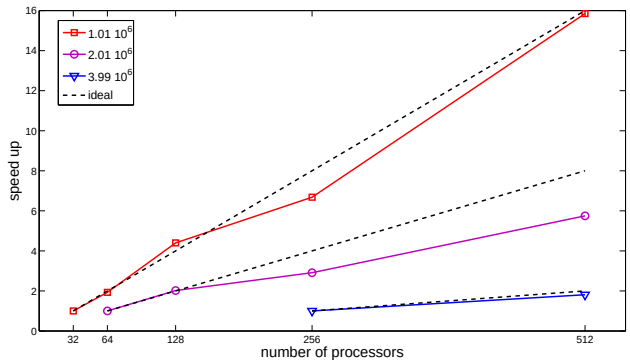

Figure 9: Speedup versus number of processors for three different grid sizes, each with the number of unknowns listed in the legend. Near ideal speedups are observed for this range of problem sizes and processor counts.

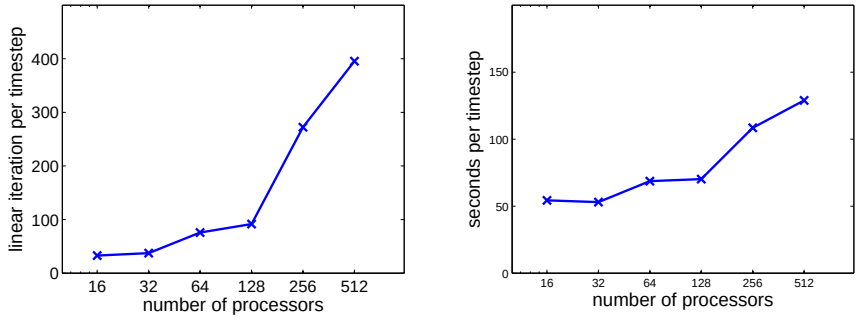

Figure 10: Weak scaling of linear solver. On the left, the vertical axis shows the average number of linear iterations per time step. On the right, the vertical axis shows the average computing time in seconds per time step. The number of unknowns increases with the number of processors: 3.99×10^6 for 512 processors, 1.01×10^6 for 128 processors and so on.

of linear iterations and the compute time, it shows that RAS has a similar performance with these two different types of outflow boundary conditions. As illustrated in the two tests, we show that RAS is a suitable choice to handle the resistance boundary condition, although the domain decomposition breaks up the connection of this integral boundary condition.

For the following tests, we study the scalability and robustness of our solver by using the resistance outflow boundary condition and restriction of Choice 1. In Fig. 9, we show the speedup over the number of processors for different grid sizes. Indeed, our algorithm shows satisfactory scalability for a range of problem sizes and with up to 512 processors. An issue of the one-level additive Schwarz method is that the preconditioning becomes weaker as the number of subdomains increases. As we can see in Fig. 10, the number of GMRES iterations per time step increases as the number of processors increases and the computing time per time step also increases. To improve the scalability, multi-level methods with coarse grids are needed.

For the overlapping additive Schwarz preconditioner, the overlap parameter δ is sig-

Table 3: The effect of various choices of the overlap parameter δ on different grid sizes and numbers of processors. A large overlap helps to reduce the number of linear iterations, but costs more communication time. The optimal choice of δ in each case is highlighted with a^*.

unknowns	np	overlap δ	Newton	GMRES	time (s)
1.01×10^6	64	2	3.0	33.5	153.88*
1.01×10^6	64	4	3.0	22.3	160.27
1.01×10^6	64	6	3.0	17.9	166.81
1.01×10^6	64	8	3.0	15.7	193.38
1.01×10^6	128	2	3.0	44.6	64.02*
1.01×10^6	128	4	3.0	30.5	70.23
1.01×10^6	128	6	3.0	24.6	79.27
1.01×10^6	128	8	3.0	21.8	90.99
1.01×10^6	256	2	3.0	65.7	33.24*
1.01×10^6	256	4	3.0	42.1	46.33
1.01×10^6	256	6	3.0	33.4	42.80
1.01×10^6	256	8	3.0	29.5	49.03
2.01×10^6	128	2	3.0	95.3	159.22
2.01×10^6	128	4	3.0	54.7	156.53*
2.01×10^6	128	6	3.0	42.6	184.81
2.01×10^6	128	8	3.0	34.8	264.50
2.01×10^6	256	2	3.1	153.5	89.75*
2.01×10^6	256	4	3.0	90.7	108.77
2.01×10^6	256	6	3.0	57.9	113.67
2.01×10^6	256	8	3.0	46.2	107.89
2.01×10^6	512	2	3.4	292.6	64.29
2.01×10^6	512	4	3.0	162.8	54.96*
2.01×10^6	512	6	3.0	114.8	57.97
2.01×10^6	512	8	3.1	69.8	79.04
3.99×10^6	256	2	3.0	122.5	198.65
3.99×10^6	256	4	3.0	69.0	188.95*
3.99×10^6	256	6	3.0	53.8	201.79
3.99×10^6	256	8	3.0	45.9	224.53
3.99×10^6	512	2	3.0	269.1	120.40
3.99×10^6	512	4	3.0	131.8	128.94
3.99×10^6	512	6	3.0	89.3	111.43*
3.99×10^6	512	8	3.0	67.3	127.36

nificant to the convergence of the linear solver. Large δ corresponds to a better preconditioner and fewer linear iterations. However, large δ also costs more communications. It is always a trade off to choose the parameter δ, as we show in Table 3.

Since the temporal discretization in our solver is fully implicit, our solver is robust with respect to different time step sizes, see Table 4.

There are two important physical parameters in describing the properties of the elastic artery walls, the Young's modulus E and the Poisson ratio ν. The Young's modulus

Table 4: Performance for various time step sizes Δt.

unknowns	np	Δt (s)	Newton	GMRES	time (s)
1.01×10^6	256	1.0×10^{-3}	3.0	42.1	46.39
1.01×10^6	256	2.5×10^{-3}	3.5	55.5	57.36
1.01×10^6	256	5.0×10^{-3}	4.3	56.0	69.79
2.01×10^6	512	1.0×10^{-3}	3.0	162.1	54.82
2.01×10^6	512	2.5×10^{-3}	4.0	262.5	92.63
2.01×10^6	512	5.0×10^{-3}	4.8	322.7	127.70

Table 5: Performance for various values of Young's modulus E_s.

unknowns	np	E_s (g/(cms^2))	Newton	GMRES	time (s)
1.01×10^6	128	6.0×10^5	3.0	30.5	70.23
1.01×10^6	128	1.4×10^6	3.0	39.0	72.54
1.01×10^6	128	6.0×10^6	3.0	59.4	77.07
1.01×10^6	256	6.0×10^5	3.0	42.1	46.33
1.01×10^6	256	1.4×10^6	3.0	53.9	47.24
1.01×10^6	256	6.0×10^6	3.0	88.0	52.14
2.01×10^6	256	6.0×10^5	3.0	90.7	108.77
2.01×10^6	256	1.4×10^6	3.0	122.5	117.77
2.01×10^6	256	6.0×10^6	3.9	302.7	224.75
2.01×10^6	512	6.0×10^5	3.0	162.1	54.96
2.01×10^6	512	1.4×10^6	3.1	225.9	66.69
2.01×10^6	512	6.0×10^6	4.0	452.9	130.21

Table 6: Performance for various values of the Poisson ratio ν. Increasing the Poisson ratio has only moderate effect to our solver.

unknowns	np	ν	Newton	GMRES	time (s)
1.01×10^6	128	0.40	3.0	28.0	69.86
1.01×10^6	128	0.45	3.0	29.0	70.55
1.01×10^6	128	0.48	3.0	29.6	70.09
2.01×10^6	256	0.40	3.0	65.5	101.91
2.01×10^6	256	0.45	3.0	72.2	104.70
2.01×10^6	256	0.48	3.0	88.6	108.27
3.99×10^6	512	0.40	3.0	110.1	123.13
3.99×10^6	512	0.45	3.0	117.3	125.05
3.99×10^6	512	0.48	3.0	129.5	128.26

is related to the stiffness of the elastic structure, while the Poisson ratio is a parameter representing the incompressibility of the structure. Generally speaking, stiffer structure (higher Young's modulus) and greater Poisson Ratio (the incompressible limit is 0.5) increases the difficulty of the simulation. Our solver shows robustness to both parameters, see Table 5 and Table 6.

Table 7: Performance for various Reynolds numbers. The tests are run on a fixed grid with 2.01×10^6 degrees of freedom and 256 processors.

Re	inlet velocity (cm/s)	viscosity $(\mathrm{g}/(\mathrm{cm}\cdot\mathrm{s}))$	Newton	GMRES	time (s)
143	5.0	0.035	3.7	83.0	136.15
286	10.0	0.035	3.9	82.2	138.27
429	15.0	0.035	4.0	80.6	140.77
500	5.0	0.01	3.6	75.7	129.62
1000	10.0	0.01	3.9	76.0	136.88
1500	15.0	0.01	3.9	74.0	135.72

Table 8: Performance for different combinations of fluid density ρ_f and solid density ρ_s. Dynamic viscosity μ_f is kept as $3.5\times10^{-3}\mathrm{g}/(\mathrm{cm}\cdot\mathrm{s})$. The tests are run on a fixed grid with 2.01×10^6 degrees of freedom and 256 processors.

ρ_f $(\mathrm{g}/\mathrm{cm}^3)$	ρ_s $(\mathrm{g}/\mathrm{cm}^3)$	Newton	GMRES	time (s)
0.1	1.0	3.6	296.9	204.60
1.0	1.0	3.0	92.0	109.77
10.0	1.0	3.5	55.9	116.36
100.0	1.0	3.9	51.1	131.34
1.0	0.01	3.1	128.8	122.62
1.0	0.1	3.1	121.4	120.87
1.0	10.0	3.0	61.4	101.59
1.0	100.0	3.0	73.1	104.88

In our model, the blood is modeled as a Newtonian viscous fluid. The Reynolds number is determined by $Re=(\rho_f\bar{V}D)/\mu_f$, where $\bar{V}$ is the characteristic velocity, D is the characteristic velocity and μ_f is the dynamic viscosity. Shown in Table 7, our algorithm performs well for various Reynolds numbers and is not so sensitive to the dynamic viscosity μ_f and the characteristic velocity $\bar{V}$.

In the iterative coupling approach for fluid-structure interaction problems, the added mass effect sometimes is a serious issue; i.e., the convergence becomes more difficult to achieve if the density of the fluid and the structure are close to each other [9]. As one can see in Table 8, our fully coupled approach has good convergence regardless of the density of fluid and structure.

5 Conclusions

In this paper, we studied and implemented a parallel domain decomposition algorithm for simulating blood flows in complaint arteries with the resistive outflow boundary condition and showed by a large number of numerical experiments that the resistive outflow boundary condition is an improvement over the zero-traction outflow boundary condition. We also discussed the performance of the overlapping additive Schwarz preconditioner to the integral type resistive boundary condition. In addition, our algorithm is

shown to be scalable on a large scale supercomputer and robust with respect to several important physical and numerical parameters.

Acknowledgments

Special thanks to Andrew Barker for his previous work on this project and to Zhenbi Su, Kendall Hunter and Robin Shandas for helpful discussions and acquiring clinical data for our model.

References

[1] S. Badia, A. Quaini and A. Quarteroni, Splitting methods based on algebraic factorization for fluid-structure interaction, SIAM J. Sci. Comput., 30 (2008), 1778–1805.
[2] S. Balay, K. Buschelman, V. Eijkhout, W. D. Gropp, D. Kaushik, M. G. Knepley, L. C. McInnes, B. F. Smith and H. Zhang, PETSc users manual, Technical report, Argonne National Laboratory, 2010.
[3] A. T. Barker, Monolithic Fluid-Structure Interaction Algorithms for Parallel Computing with Application to Blood Flow, PhD thesis, University of Colorado at Boulder, 2009.
[4] A. T. Barker and X.-C. Cai, Scalable parallel methods for monolithic coupling in fluid-structure interaction with application to blood flow modeling, J. Comput. Phys., 229 (2010), 642–659.
[5] Y. Bazilevs, V. Calo, Y. Zhang and T. Hughes, Isogeometric fluid-structure interaction analysis with applications to arterial blood flow, Comput. Mech., 38 (2006), 310–322.
[6] Y. Bazilevs, V. Calo, T. Hughes and Y. Zhang, Isogeometric fluid-structure interaction: theory, algorithms and computations, Comput. Mech., 43 (2008), 3–37.
[7] X.-C. Cai, W. D. Gropp, D. E. Keyes, R. G. Melvin and D. P. Young, Parallel Newton-Krylov-Schwarz algorithms for the transonic full potential equation, SIAM J. Sci. Comput., 19 (1998), 246–265.
[8] X.-C. Cai and M. Sarkis, A restricted additive Schwarz preconditioner for general sparse linear systems, SIAM J. Sci. Comput., 21 (1999), 792–797.
[9] P. Causin, J. F. Gerbeau and F. Nobile, Added-mass effect in the design of partitioned algorithms for fluid-structure problems, Comput. Methods Appl. Mech. Eng., 194 (2005), 4506–4527.
[10] J. E. Dennis Jr. and R. B. Schnabel, Numerical Methods for Unconstrained Optimization and Nonlinear Equations, Society for Industrial and Applied Mathematics, Philadelphia, 1996.
[11] J. Donea, S. Giuliani and J. P. Halleux, An arbitrary Lagrangian-Eulerian finite element method for transient dynamic fluid-structure interactions, Comput. Methods Appl. Mech. Eng., 33 (1982), 689–723.
[12] S. C. Eisenstat and H. F. Walker, Globally convergent inexact Newton method, SIAM J. Optim., 4 (1994), 393–422.
[13] S. C. Eisenstat and H. F. Walker, Choosing the forcing terms in an inexact Newton method, SIAM J. Sci. Comput., 17 (1996), 16–32.
[14] C. Farhat and P. Geuzaine, Design and analysis of robust ALE time-integrators for the solution of unsteady flow problems on moving grids, Comput. Methods Appl. Mech. Eng., 193 (2004), 4073–4095.

[15] C. Farhat, P. Geuzaine and C. Grandmont, The discrete geometric conservation law and the nonlinear stability of ALE schemes for the solution of flow problems on moving grids, J. Comput. Phys., 174 (2001), 669–694.
[16] C. A. Figueroa, I. E. Vignon-Clementel, K. E. Jansen, T. J. R. Hughes and C. A. Taylor, A coupled momentum method for modeling blood flow in three-dimensional deformable arteries, Comput. Methods Appl. Mech. Eng., 195 (2006), 5685–5706.
[17] L. Formaggia, J. F. Gerbeau, F. Nobile and A. Quarteroni, On the coupling of 3D and 1D Navier-Stokes equations for flow problems in compliant vessels, Comput. Methods Appl. Mech. Eng., 191 (2001), 561–582.
[18] Y. C. Fung, Biomechanics: Circulation, 2nd edition, Springer-Verlag, New York, 1997.
[19] M. Heil, An efficient solver for the fully coupled solution of large-displacement fluid-structure interaction problems, Comput. Methods Appl. Mech. Eng., 193 (2004), 1–23.
[20] T. J. R. Hughes, W. K. Liu and T. K. Zimmermann, Lagrangian-Eulerian finite element formulation for incompressible viscous flows, Comput. Methods Appl. Mech. Eng., 29 (1981), 329–349.
[21] F.-N. Hwang and X.-C. Cai, A parallel nonlinear additive Schwarz preconditioned inexact Newton algorithm for incompressible Navier-Stokes equations, J. Comput. Phys., 204 (2005), 666–691.
[22] G. Karypis, R. Aggarwal, K. Schloegel, V. Kumar and S. Shekhar, METIS/ParMETIS web page, University of Minnesota, 2010, `http://glaros.dtc.umn.edu/gkhome/views/metis`.
[23] P. Le Tallec and J. Mouro, Fluid structure interaction with large structural displacements, Comput. Methods Appl. Mech. Eng., 190 (2001), 3039–3067.
[24] C. Michler, E. H. van Brummelen, S. J. Hulshoff and R. de Borst, The relevance of conservation for stability and accuracy of numerical methods for fluid-structure interaction, Comput. Methods Appl. Mech. Eng., 192 (2003), 4195–4215.
[25] W. W. Nichols and M. F. O'Rourke, McDonald's Blood Flow in Arteries: Theoretical, Experimental and Clinical Principles, Oxford University Press, New York, 1998.
[26] F. Nobile, Numerical Approximation of Fluid-Structure Interaction Problems with Application to Haemodynamics, PhD thesis, Ecole Polytechnique Federade Lausanne, 2001.
[27] S. J. Owen and J. F. Shepherd, CUBIT project web page, Sandia National Laboratories, 2010, `http://cubit.sandia.gov/`.
[28] S. Piperno and C. Farhat, Partitioned procedures for the transient solution of coupled aeroelastic problems-part II: energy transfer analysis and three-dimensional applications, Comput. Methods Appl. Mech. Eng., 190 (2001), 3147–3170.
[29] Y. Saad and M. H. Schultz, GMRES: A generalized minimal residual algorithm for solving nonsysmetric linear system, SIAM J. Sci. Stat. Comput., 7 (1986), 856–869.
[30] C. A. Taylor and M. T. Draney, Experimental and computational methods in cardiovascular fluid mechanics, Ann. Rev. Fluid Mech., 36 (2004), 197–231.
[31] C. A. Taylor and J. D. Humphrey, Open problems in computational vascular biomechanics: hemodynamics and arterial wall mechanics, Comput. Methods Appl. Mech. Eng., 198 (2009), 3514–3523.
[32] I. E. Vignon and C. A. Taylor, Outflow boundary conditions for one-dimensional finite element modeling of blood flow and pressure waves in arteries, Wave Motion, 39 (2004), 361–374.
[33] I. E. Vignon-Clementel, C. A. Figueroa, K. E. Jansen and C. A. Taylor, Outflow boundary conditions for three-dimensional finite element modeling of blood flow and pressure in arteries, Comput. Methods Appl. Mech. Eng., 195 (2006), 3776–3796.